

## Article

# Microstructure and Corrosion Properties of Wire Arc Additively Manufactured Multi-Trace and Multilayer Stainless Steel 321

Xiaoli Wang <sup>1,\*</sup>, Qingxian Hu <sup>1,\*</sup>, Wenkang Liu <sup>1</sup>, Wei Yuan <sup>1</sup>, Xinwang Shen <sup>1</sup>, Fengyin Gao <sup>1</sup>, Douxi Tang <sup>2</sup> and Zichen Hu <sup>1</sup>

<sup>1</sup> School of Materials Science and Engineering, Jiangsu University of Science and Technology, Zhenjiang 212003, China; liuwk999@stu.just.edu.cn (W.L.); 192210601303@stu.just.edu.cn (W.Y.); 1440602222@stu.just.edu.cn (X.S.); 209060090@stu.just.edu.cn (F.G.); hzc18796016103@163.com (Z.H.)

<sup>2</sup> Shanghai Xinzhan Industrial Automation Co., Ltd., Shanghai 201600, China; 13776023330@163.com

\* Correspondence: xlwang@just.edu.cn (X.W.); huqingxian@just.edu.cn (Q.H.)

**Abstract:** Because low thermal conductivity and high viscosity are common characteristics of austenitic steel, it is easy to cause a large amount of heat accumulation in the chip area, resulting in tool edge collapse or wear, and the traditional preparation method is unsuitable for preparing large and complex austenitic steel components. Wire + arc additive manufacturing (WAAM) provides a great application value for austenitic stainless steel because it can solve this problem. The cold metal transfer (CMT)-WAAM system with good control of heat input was used to fabricate the multi-trace and multilayer stainless steel 321 (SS 321) workpiece in this study. The microstructure and corrosion properties of the SS 321 workpiece were observed and compared with those of an SS 321 sheet. The results showed that the microstructure of the SS 321 workpiece from top to bottom was regularly and periodically repeated from the overlapping remelting zone, inter-layer remelting zone, and primary melting zone. There was white austenite matrix and black ferrite, and a small amount of skeleton and worm ferrite was distributed on the white austenite matrix. The average hardness value from the top to the bottom region was approximately uniform, indicating that the workpiece had good consistency. The corrosion properties in 0.5 mol/L H<sub>2</sub>SO<sub>4</sub> solutions were compared between the SS 321 workpiece and the SS 321 sheet. The results showed that the corrosion properties of the top region of the workpiece were better than that of the middle and bottom part, and the corrosion properties of the SS 321 workpiece were better than that of the SS 321 sheet.

**Keywords:** SS 321; corrosion properties; CMT-WAAM



**Citation:** Wang, X.; Hu, Q.; Liu, W.; Yuan, W.; Shen, X.; Gao, F.; Tang, D.; Hu, Z. Microstructure and Corrosion Properties of Wire Arc Additively Manufactured Multi-Trace and Multilayer Stainless Steel 321. *Metals* **2022**, *12*, 1039. <https://doi.org/10.3390/met12061039>

Academic Editors: Hongtao Zhang and Yanan Li

Received: 15 May 2022

Accepted: 15 June 2022

Published: 17 June 2022

**Publisher's Note:** MDPI stays neutral with regard to jurisdictional claims in published maps and institutional affiliations.



**Copyright:** © 2022 by the authors. Licensee MDPI, Basel, Switzerland. This article is an open access article distributed under the terms and conditions of the Creative Commons Attribution (CC BY) license (<https://creativecommons.org/licenses/by/4.0/>).

## 1. Introduction

Because the common characteristic of austenitic steel is low thermal conductivity (10~30 W/(m·°C)) and high viscosity, there are high mechanical, temperature, and speed loads on the workpiece-tool-chip interface in the cutting process. Under the action of a certain thermal-mechanical coupling, it is easy to produce tool-chip bonding phenomenon, and it is easy to cause a large amount of heat accumulation in the chip area, which leads to the softening of the tool materials and accelerates their failure, resulting in tool edge collapse or wear. The traditional preparation method is not suitable for preparing large and complex components of austenite, while welding technology is suitable for producing complex structures involving stainless steel [1,2]. Wire + arc additive manufacturing (WAAM) is new rapid manufacturing welding technology. Compared with laser additive manufacturing [3] and electron beam additive manufacturing [4], wire + arc additive manufacturing with an arc as a heat source and welding wire as the filler material, has the advantages of high manufacturing efficiency, simple equipment, and low cost, and it is very suitable for preparing large complex components.

Many studies about austenitic stainless steel additive manufacturing have been carried out. Especially in recent years, the number of papers about WAAM austenitic stainless steel

has increased. Li et al. investigated the low cycle fatigue behavior of stainless steel 308L (SS 308L) fabricated by WAAM. The results showed that WAAM SS 308L, compared with hot-rolled SS 308L, had higher yield stress and longer fatigue life [5]. Wang et al. studied the effect of heat treatment temperature on the microstructure and tensile properties of austenitic stainless 316L (SS 316L) using WAAM [6]. Van Thao Le et al. [7] studied the microstructure and mechanical properties of 308L fabricated by the gas metal arc welding (GMAW) additive manufacturing. These researchers mainly studied the mechanical properties of stainless-steel additive manufacturing. Palmeira Belotti et al. [8] studied the microstructural characterization of thick-walled SS 316L made by WAAM. The results showed an oriented and textured structure with large grains at the overlapping region of adjacent fusion zones. Mohan Kumar et al. studied the high-temperature performance of an SS 321 wall manufactured by WAAM [9]. Oliveira et al. [10,11] studied the effect of contaminations and heat treatments on 316L fabricated by WAAM. Most of these studies focused on the mechanical properties of SS 308L and SS 316L. There were few studies on SS 321 additive manufacturing.

Because 321 stainless steel has poor thermal conductivity and strong liquid metal fluidity, it is easy to produce heat accumulation in additive manufacturing, resulting in inflow and collapse. However, there are ways to mitigate this. It is critical to select the appropriate additive manufacturing system, and the heat input cannot be too large. Cold metal transfer (CMT) melting technology does well on the heat input control and steady transfer model [12]. A CMT-WAAM system was selected in this work.

The research of SS 321 fabricated by additive manufacturing mainly focused on the microstructure and corrosion behavior in a neutral chloride ion environment [13,14]. In fact, SS 321 is widely used in the petrochemical industry, nuclear reactors, aircraft engine exhaust systems, and other high-temperature fields. It is also commonly used in power plants and other enterprises as flue gas desulfurization anode plates. The flue gas contains SO<sub>2</sub> and SO. When the flue gas is cooled and dewed on the anode plate, it will condense out, leading to the corrosion of the components. The SO<sub>2</sub> reacts with water to produce H<sub>3</sub>SO<sub>2</sub>. Finally, sulfuric acid is generated under the action of oxygen. The anode plate is corroded to failure under the action of sulfuric acid. Therefore, to the study of the corrosion behavior of SS 321 in sulfuric acid has practical significance. However, no research work has been reported on the corrosion properties of SS 321 in an acidic environment. In this work, the microstructure and hardness of an SS 321 workpiece fabricated by a CMT-WAAM system was studied. The corrosion properties of SS 321 and an SS 321 sheet in 0.5 mol/L H<sub>2</sub>SO<sub>4</sub> solutions was reviewed to provide theoretical reference and data support for the application of SS 321 in an acidic medium.

## 2. Materials and Methods

### 2.1. Materials

The chemical composition of ER321 feeding wire and SS 321 sheet are shown in Table 1.

**Table 1.** Chemical composition of ER321 feeding wire and SS 321 sheet (wt.%).

Element	C	Si	Mn	Ni	Ti	Cr	Mo	Fe
ER321 wire	0.08	0.50	1.47	9.10	0.50	19.05	≤0.075	Bal.
SS 321 sheet	0.05	0.75	1.50	9.10	0.50	17.1	/	Bal.

Figure 1 shows the microstructure of the SS 321 sheet. The distribution and size of austenite grains were uniform. There was a strip of ferrite between the austenite grains.

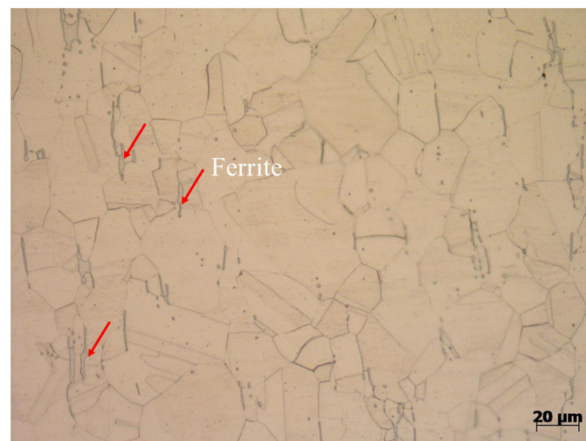


**Figure 1.** Optical microstructure of SS 321 sheet.

## 2.2. Experimental System and Process Parameters

The CMT-WAAM system consisted of a welding power supply (TPS 4000), a robot, and a gas cylinder, as shown in Figure 2a, and the deposition direction along Y axis. The traveling direction of the CMT-WAAM system is shown in Figure 2b. The cross-section diagram of the CMT-WAAM SS 321 workpiece is shown in Figure 2c. The test samples were extracted from the top, middle, and bottom of the CMT-WAAM SS 321 workpiece. In the process of the SS 321 additive manufacturing, the value of current was 150–170 A and that of power was 18.1 V. The printing speed was 13–16 mm·s<sup>-1</sup>. The preheating temperature was 30–50 °C, and the interlayer temperature was ≤100 °C. The dry extension was 10–15 mm, and the inter-channel offset was 3–3.5 mm. The shielding gas was a 90% Ar and 10% He premix at a gas flow of 15–20 L·min<sup>-1</sup>.

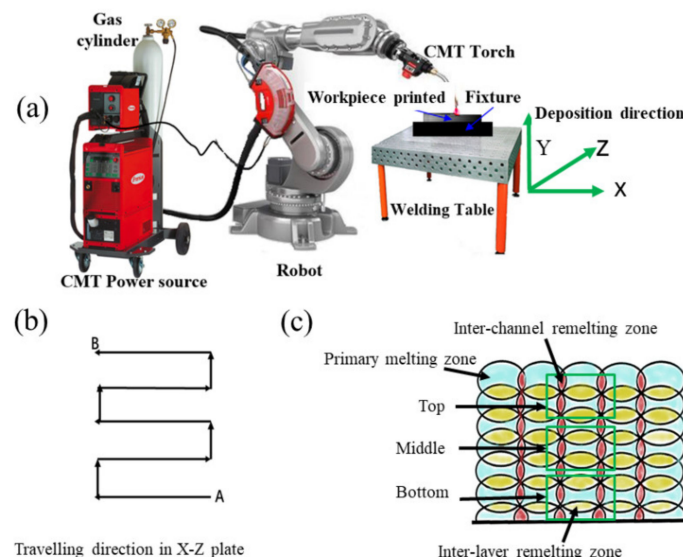


**Figure 2.** Schematic diagram of wire arc additively manufactured SS 321 by a CMT-WAAM system (a), the traveling (b), and the diagram of section and the sampling position of the SS 321 workpiece (c).

## 2.3. Microstructure Observation and Performance Test

The test samples and the size were extracted from the top, middle, and bottom parts of the SS 321 workpiece, as shown in Figure 2c, and the size was 10 mm × 10 mm × 5 mm. For comparative analysis, the SS 321 plate was cut into samples of the same size, named SS 321 sheet. They were ground with 240, 600, and 1000 mesh silicon carbide papers, in turn, and then were mechanically polished with 2.5 μm diamond polishing paste for microstructure observation, hardness test, and electrochemical test.

The microstructures of samples were observed by an optical microscope (Nikon Epiphot 300 model, Tokyo, Japan). The hardness test was carried out by a DHV-1000 hardness test (Shanghai Shangcai Tester Machine, Co., Ltd., Shanghai, China). The test point interval was 0.5 mm, the load was 500 g, and the holding time was 10 s.

A Corrtest CS2350 electrochemical workstation was used to carry out the electrochemical experiments at  $23 \pm 1$  °C. The experimental medium was 0.5 mol H<sub>2</sub>SO<sub>4</sub> solution, and it was made of analytical-grade 97% H<sub>2</sub>SO<sub>4</sub> and distilled water. A three-electrode system was adopted for the electrochemical tests. The polishing sample to be tested was the working electrode, a Pt electrode was the auxiliary electrode, and a saturated calomel electrode was the reference electrode. To achieve a steady-state and gain open-circuit potential (OCP), the working electrodes (sample) were tested over time for 30 min. The experiments stopped when the current density reached 20 Ma/cm<sup>2</sup>. Each test was repeated three times for the reliability of the experimental data.

The corrosion morphology and the element analyses were performed using a field emission scanning electron microscope (SU-70) (Hitachi, Tokyo, Japan).

### 3. Results and Discussions

#### 3.1. Macroscopic and Microstructure Observation

Figure 3 shows the overall macro morphology of the SS 321 workpiece formed by the CMT-WAAM process. The workpiece had a surface with a corrugated morphology. The weld bead was compact, free of cracks and visual defects.



**Figure 3.** Macroscopic morphology of SS 321 fabricated by CMT-WAAM.

#### 3.2. Microstructure Observation

Figure 4 shows the microstructure between welding traces of the SS 321 workpiece. Figure 4(a,a1,a2), Figure 4(b,b1,b2) and Figure 4(c,c1,c2) are the metallographic structures of the top, middle, and bottom samples, respectively. The microstructure of the three pieces from top to bottom was regularly and periodically repeated from the overlapping remelting zone, inter-layer remelting zone, and primary melting zone. As shown in Figure 2c, the blue parts represent primary melting zones. The red parts represent the overlapping area of the two welding passes, namely the overlapping remelting zones, and the yellow details represent the overlapping area between the upper layer and the lower layer, namely the inter-layer remelting zones. Compared with the top, middle, and bottom samples in Figure 4a–c, the overlapping remelting zone and the inter-layer remelting zone of the middle piece were smaller and narrower. The microstructures of the SS 321 workpiece in each region were similar. Its structure consisted of cellular and dendritic crystals. The bright areas were austenite, while the dark areas were ferrite. According to Schaeffler's diagram and the empirical formulas for nickel equivalent (Ni<sub>eq</sub>) and chromium equivalent (Cr<sub>eq</sub>) [15,16],

$$\text{Creq} = \text{Cr} + \text{Mo} + 1.5 \text{ Si} \quad (1)$$

$$\text{Nieq} = \text{Ni} + 30 \text{ C} + 0.5 \text{ Mn} \quad (2)$$

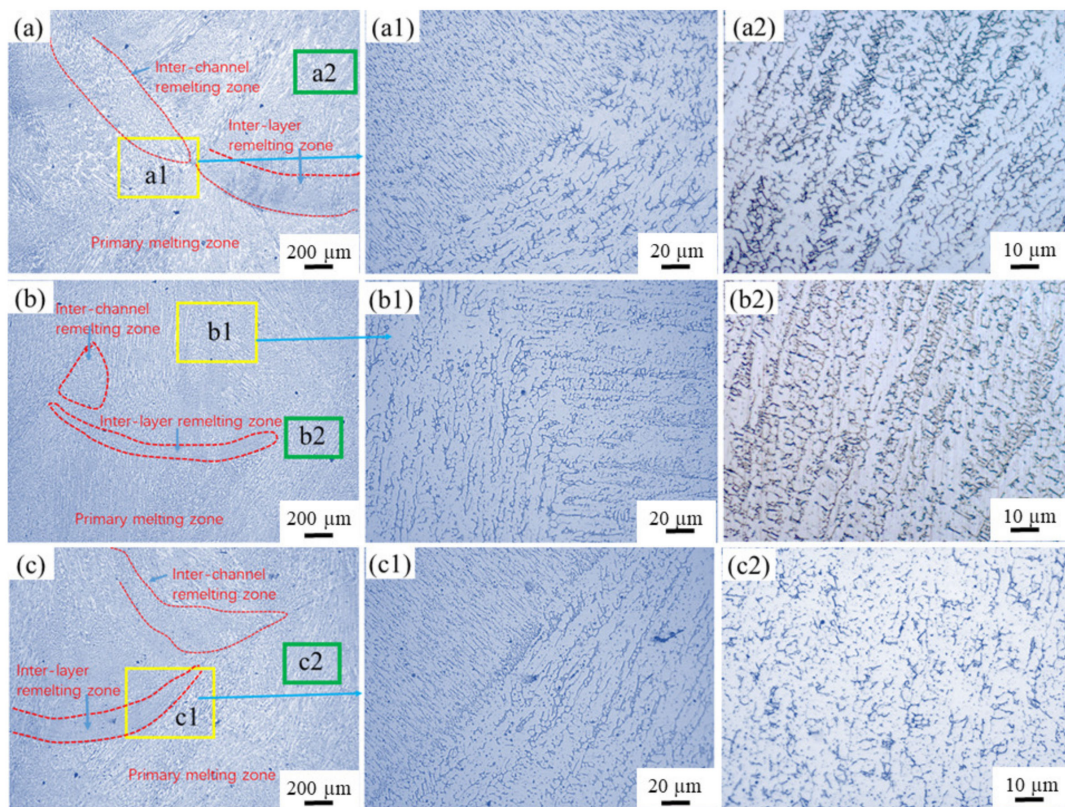


**Figure 4.** Microstructure between welding traces of 321 stainless steel printed workpiece. (a–c,a1–c1,a2–c2) are the metallographic structures of the top, middle, and bottom samples, respectively.

The value of  $C_{req}/N_{ieq}$  of the element composition of ER321 wire listed in Table 1 was 1.75. The solidification mode of the SS 321 workpiece belonged to the FA solidification mode. The solidification process was as follows: after the molten metal was successfully spread in the appropriate position, the heat flow and the liquid temperature of the metal was reduced to the solid-liquid two-phase region, and the  $\delta$  ferrite was preferentially precipitated from the liquid phase. When the temperature continued to decrease to the solid line, the  $\delta$  ferrite gradually transformed to  $\gamma$  austenite. The first precipitated ferrite matrix was swallowed by the new austenite. Due to the rapid cooling rate of the weld metal, the  $\gamma$  austenite still contained untransformed complete  $\delta$  ferrite when fully solidified.

There were equiaxed grains or more refined structures on the interface between the two welding passes. The upper layer crystallized vertically to the lower layer, as shown in Figure 4a1,b1, or at a certain angle with the adjacent weld pass, as shown in Figure 4c1.

A small amount of skeleton and worm ferrite was distributed on a white austenite matrix. Figure 4a2 shows that the metallographic structure of the top sample had columnar dendrites and equiaxed crystals. When the last layer was completed, the heat accumulation of the whole workpiece reached the maximum, and the temperature gradient in the vertical direction was the smallest. Since the top layer would not be subjected to subsequent multiple heating cycles, at this time, the heat loss was more likely to be perpendicular to the direction of the weld pass. Therefore, the growth direction of the dendrite would change from perpendicular to the bottom plate to perpendicular to the weld pass. Namely, the dendrite orientation deflection phenomenon occurred. At the top of the workpiece, the welding passes directly contacted with air, and the heat dissipation trend along the whole top surface was balanced with that along the vertical surface. Under this balance, the crystallization state changed from columnar dendrite to equiaxed dendrite. The microstructure of the middle sample is shown in Figure 4b2. It showed that dendrite had

obvious directionality, and majority of the  $\delta$  ferrite appeared in worm morphology rather than in the skeleton one. Xiaohui et al. [17] studied 316L stainless steel fabricated by GTAW-WAAM. The results showed that many austenitic dendrites were vertically distributed in the well-formed 316L components, and large columnar grains were formed in the middle region. The microstructure of the members was composed of  $\delta$ ,  $\gamma$ , and  $\delta$  phases. The  $\delta$  phase first exhibited a network morphology in austenite dendrites. As the deposition layer was affected by thermal cycles, the  $\delta$  phase gradually dissolved in austenite and became worm morphology. Secondary dendrites were underdeveloped, and their microstructure was the smallest in Figure 4c2. The continuity of skeleton  $\delta$  ferrite was poor, the dendrite orientation was slightly disordered, and the secondary dendrite was developed, weakening the directionality of columnar and dendritic austenites, preventing continuous network chromium carbide precipitation at austenite grain boundaries from intergranular corrosion.

### 3.3. Hardness Analysis

The curves of hardness and average hardness are shown in Figure 5. The hardness of the four samples showed fluctuation. The hardness fluctuation of 321 steel additive manufacturing samples may be due to the continuous heating of the deposition layer, which caused slight development of the  $\delta$  ferrite phase due to the facilitation of solute elements' redistribution during the additive manufacturing process [18]. It can be seen from Figure 4 that a small amount of austenite fine grains appeared in the interlayer fusion zone, which also causes fluctuation of the hardness value. The average hardness value of the SS 321 sheet was 198 HV. For the SS 321 workpiece, the Vickers hardness increased with distance from the bottom plate, but the hardness range was not extensive, indicating that this WAAM workpiece had good consistency. This result was consistent with our other WAAM stainless steel [19]. The maximum average hardness of the WAAM SS 321 workpiece was 202 HV, while the maximum hardness of the SS 321 sample fabricated by electron beam was 198 HV [20].

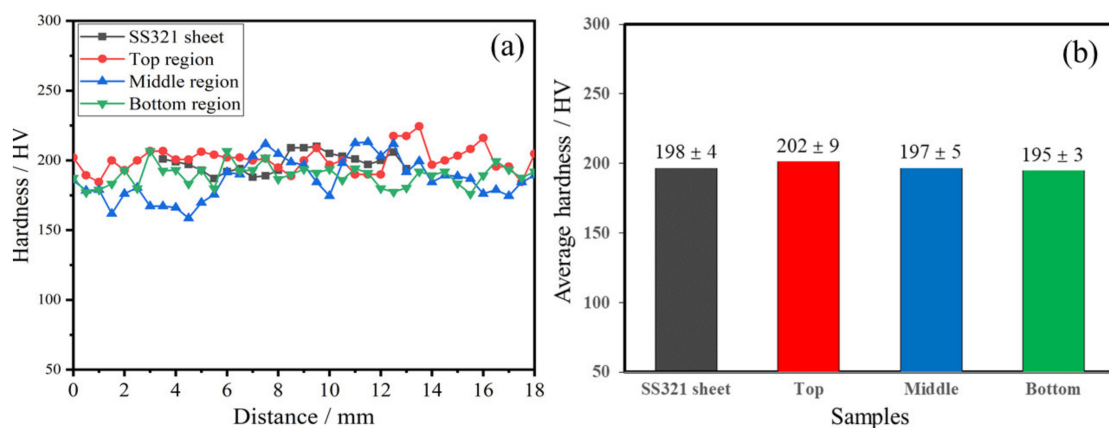


**Figure 5.** Curves of hardness (a) and average hardness (b) of SS 321 sheet, the top region, middle region, and bottom region of the SS 321 workpiece.

### 3.4. Corrosion Behavior of Samples

#### 3.4.1. OCP Measurements of Samples

Figure 6 shows the changing trend of the open-circuit potential (OCP) curves of the SS 321 sheet and different regions of the SS 321 WAAM in 0.5 mol/L  $H_2SO_4$  solutions. Figure 6 displays that the OCP of the four samples shifted in the positive direction with an increasing immersion time. It reached a steady-state potential when the immersion time was 1500 s. These results indicate that the passive film formed spontaneously on the surface of the four samples [21]. The steady-state potentials of the SS 321 sheet and the top, middle, and bottom regions of the SS 321 workpiece were  $-0.11 V_{SCE}$ ,  $-0.025 V_{SCE}$ ,  $-0.075 V_{SCE}$ , and  $-0.03 V_{SCE}$ , respectively.

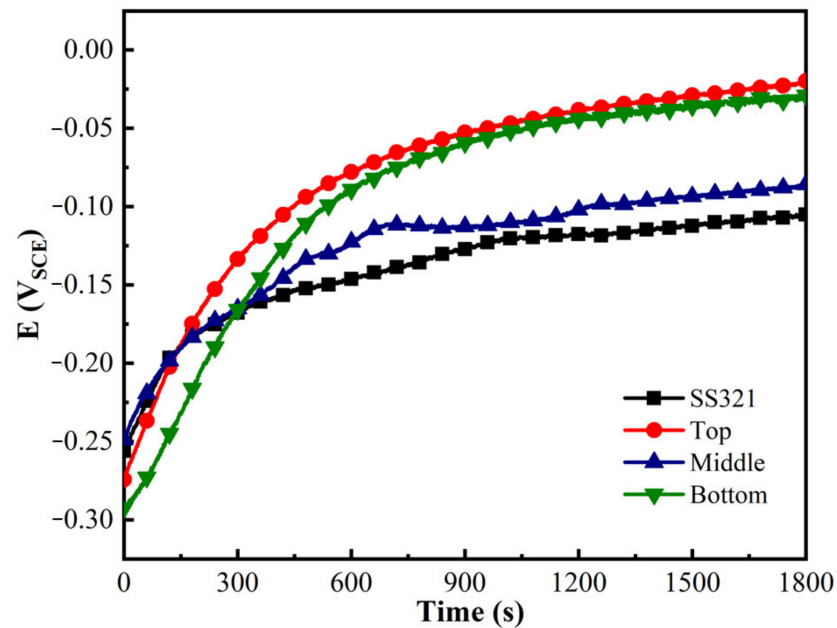


Figure 6. OCP curves of samples with immersion time in 0.5 mol/L  $\text{H}_2\text{SO}_4$  solution.

#### 3.4.2. Potentiodynamic Polarization Tests of Samples

Figure 7 displays the potentiodynamic polarization curves of the SS 321 sheet and the samples extracted from the top, middle, and bottom of the SS 321 workpiece in 0.5 mol/L solutions. The corrosion behaviors of the four samples were similar, but their corrosion potential ( $E_{corr}$ ) and corrosion current density ( $i_{corr}$ ) were notably different. The values of  $E_{corr}$  and  $i_{corr}$  extracted from Figure 7 are listed in Table 2. The  $i_{corr}$  values of the SS 321 sheet and the top, middle, and bottom regions of the SS 321 workpiece were  $(7.54 \pm 0.16) \times 10^{-7} \text{ A}\cdot\text{cm}^{-2}$ ,  $(1.65 \pm 0.19) \times 10^{-7} \text{ A}\cdot\text{cm}^{-2}$ ,  $(5.63 \pm 0.24) \times 10^{-7} \text{ A}\cdot\text{cm}^{-2}$ , and  $(3.85 \pm 0.12) \times 10^{-7} \text{ A}\cdot\text{cm}^{-2}$ , respectively. The results showed that the corrosion properties of the top region of the workpiece were better than that of the middle and bottom region, and the corrosion properties of the SS 321 workpiece were better than that of the SS 321 sheet.

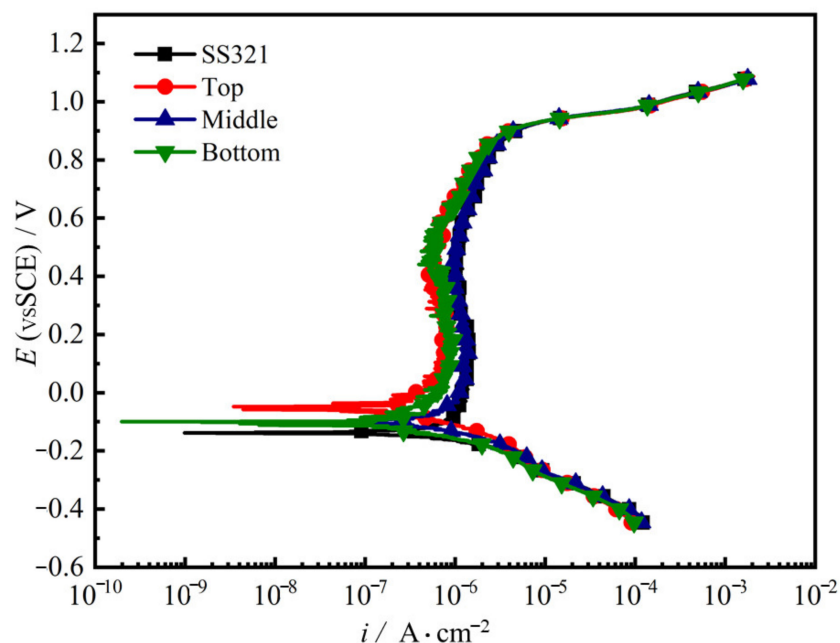
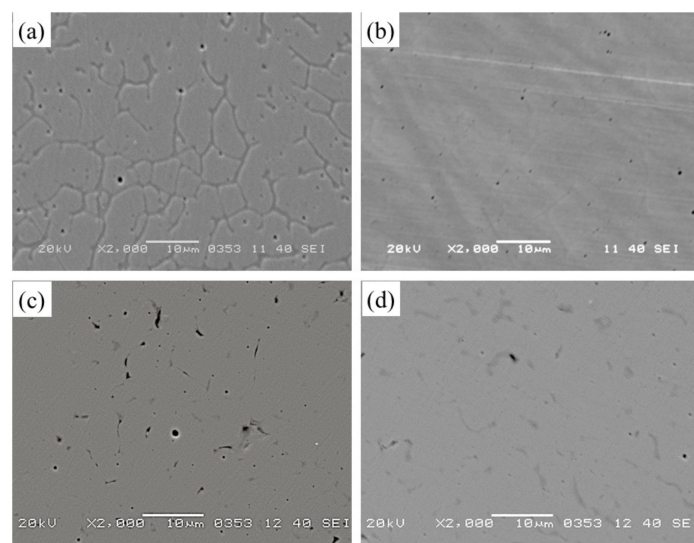


Figure 7. Potentiodynamic polarization curves of samples in 0.5 mol  $\text{H}_2\text{SO}_4$  solution.

Figure 8 shows the surface morphologies of a corroded SS 321 sheet (Figure 8a) and different regions of SS 321 workpiece printed. Figure 8b–d are the surface morphologies of the corroded top, middle, and bottom regions, respectively. It can be seen from Figure 8a that the grain boundary of the SS 321 sheet had slight corrosion, and pitting corrosion occurred near the grain boundary. A small amount of ferrite harmed the grain boundary corrosion resistance of the SS 321 sheet. Figure 8b shows that there was no obvious intergranular corrosion, only a small amount of pitting corrosion in the top region of the SS 321 workpiece. Figure 8c shows there was a tiny amount of intergranular corrosion and pitting corrosion in the middle region. Figure 8d displays that there was a bit intergranular corrosion and little pitting corrosion in the bottom region. Due to the effect of repeated thermal cycles in the middle and bottom of the SS 321, it was easy to precipitate continuous-network chromium-rich  $(Cr, Fe)_{23}C_6$  along the grain boundary at the sensitization temperature range. Thus, the matrix around the grain boundaries produced a chromium-poor zone, resulting in intergranular corrosion. Therefore, compared with the SS 321 sheet, the SS 321 workpiece had excellent intergranular corrosion resistance. The reason was that in the SS 321 workpiece, ferrite was dispersed and uniformly distributed between austenite, which weakened the direction of columnar and dendritic crystals of austenite and prevented continuous-network chromium carbide precipitation at the austenite grain boundaries, to avoid intergranular corrosion. This was attributed to the slow cooling rate, and the austenite was easy to homogenize. Therefore, in the SS 321 workpiece, ferrite was beneficial to improve resistance to intergranular corrosion.



**Figure 8.** Surface morphologies of corroded SS 321 sheet (a), and samples (b), (c), and (d) extracted from the top, middle, and bottom regions of the SS 321, respectively.

**Table 2.** Parameters extracted from potentiodynamic polarization curves (Figure 6).

	$E_{corr}$ (mV <sub>SCE</sub> )	$i_{corr}$ ( $\times 10^{-7}$ A·cm <sup>-2</sup> )
SS 321 sheet	$-138.14 \pm 4.56$	$7.54 \pm 0.16$
Top	$-53.18 \pm 1.57$	$1.65 \pm 0.19$
Middle	$-100.75 \pm 1.77$	$5.63 \pm 0.24$
Bottom	$-97.11 \pm 2.06$	$3.85 \pm 0.12$

#### 4. Conclusions

In this work, the microstructure and corrosion properties of the multi-trace and multi-layer stainless-steel 321 workpiece fabricated by the CMT-WAAM system were studied. The results showed that the microstructure of the SS 321 workpiece from top to bottom was regularly and periodically repeated from the overlapping remelting zone to the inter-layer

remelting zone, and the primary melting zone. There were a white austenite matrix and black ferrite, and a small amount of skeleton and worm ferrite was distributed on the white austenite matrix. The average hardness value from the top to the bottom region was approximately uniform, indicating that the SS 321 workpiece had good consistency. The corrosion properties of the SS 321 workpiece and the SS 321 sheet were studied in 0.5 mol/L H<sub>2</sub>SO<sub>4</sub> solutions. The results showed that the corrosion properties of the top region of the workpiece were better than that of the middle and bottom region, and the corrosion properties of the SS 321 workpiece were better than that of the SS 321 sheet. The reason was that, in the SS 321 workpiece, ferrite was dispersed and uniformly distributed between austenite, which weakened the direction of the columnar and dendritic crystals of austenite and prevented continuous-network chromium carbide precipitation at the austenite grain boundaries, to avoid intergranular corrosion. Ferrite in the SS 321 workpiece was beneficial to improve the resistance to intergranular corrosion.

**Author Contributions:** Project administration, X.W. and Q.H.; data curation, W.L., W.Y. and X.S.; formal analysis, F.G., D.T. and Z.H. All authors have read and agreed to the published version of the manuscript.

**Funding:** The National Science Foundation of China (Nos. 51675249), the Doctoral Research Fund of Jiangsu University of Science and Technology (Nos. 1062931604) supported this research.

**Institutional Review Board Statement:** Not applicable.

**Informed Consent Statement:** Not applicable.

**Data Availability Statement:** The data used to support the findings of this study are available from the corresponding authors upon request.

**Conflicts of Interest:** The authors declare no conflict of interest.

## References

1. Oliveira, J.P.; Shamsolhodaei, B.; Shen, J.J.; Lope, J.G.; Goncalves, R.M.; Ferraz, M.B. Improving the ductility in laser welded joints of CoCrFeMnNi high entropy alloy to 316 stainless steel. *Mater. Des.* **2022**, *219*, 110717. [[CrossRef](#)]
2. Oliveira, J.P.; Shen, J.J.; Zeng, Z.; Park, J.M.P.; Choi, Y.T.; Schell, N.; Maawad, E.; Zhou, N.; Kim, H.S. Dissimilar laser welding of a CoCrFeMnNi high entropy alloy to 316 stainless steel. *Scr. Mater.* **2022**, *206*, 114219. [[CrossRef](#)]
3. Zhang, H.; Li, C.; Xu, M.; Dai, W.; Kumar, P.; Liu, Z.; Li, Z.; Zhang, Y. The fatigue performance evaluation of additively manufactured 304L austenitic stainless steels. *Mater. Sci. Eng.* **2021**, *802*, 140640. [[CrossRef](#)]
4. Wang, C.; Tan, X.; Liu, E.; Tor, S.B. Process parameter optimization and mechanical properties for additively manufactured stainless steel 316L parts by selective electron beam melting. *Mater. Des.* **2018**, *147*, 157–166. [[CrossRef](#)]
5. Li, Y.J.; Yuan, Y.T.; Wang, D.X.; Fu, S.C.; Song, D.R.; Vedani, M.; Chen, X. Low cycle fatigue behavior of wire arc additive manufactured and solution annealed 308L stainless steel. *Addit. Manuf.* **2022**, *52*, 102688.
6. Wang, C.; Zhu, P.; Lu, Y.H.; Shoji, T. Effect of heat treatment temperature on microstructure and tensile properties of austenitic stainless 316L using wire and arc additive manufacturing. *Mater. Sci. Eng. A* **2022**, *832*, 142446. [[CrossRef](#)]
7. Le, V.T.; Mai, D.S. Microstructural and mechanical characteristics of 308L stainless steel manufactured by gas metal arc welding-based additive manufacturing. *Mater. Lett.* **2020**, *271*, 127791. [[CrossRef](#)]
8. Palmeira Belotti, L.; Dommelen, J.A.W.V.; Geers, M.G.D.; Goulas, C.; Ya, W.; Hoefnagels, J.P.M. Microstructural characterisation of thick-walled wire arc additively manufactured stainless steel. *J. Mater. Process. Technol.* **2022**, *299*, 117373. [[CrossRef](#)]
9. Subramanian, M.K.; Rajesh Kannan, A.; Pramod, R.; Siva Shanmugam, N.; Muthu, S.M.; Dhinakaran, V. Microstructure and high temperature performance of 321 SS wall manufactured through wire + arc additive manufacturing. *Mater. Lett.* **2022**, *314*, 131913.
10. Ramalho, A.; Santos, T.G.; Bevans, B.; Smoqi, Z.; Rao, P.; Oliveira, J.P. Effect of 316L stainless steel. *Addit. Manuf.* **2022**, *51*, 102585.
11. Rodrigues, T.A.; Escobar, J.D.; Shen, J.J.; Duarte, V.R.; Ribamar, G.G.; Avila, J.A.; Maawad, E.; Schell, N.; Santos, T.G.; Oliveira, J.P. Effect of heat treatments on 316 stainless steel parts fabricated by wire and arc additive manufacturing: Microstructure and synchrotron X-ray diffraction analysis. *Addit. Manuf.* **2021**, *48*, 102428. [[CrossRef](#)]
12. Sputo, T.; Turner, J.L. *Bracing Cold-Formed Steel Structures (A Design Guide) II Cold-Formed Steel in Metal Building Systems*; American Society of Civil Engineers: Reston, VA, USA, 2005; pp. 47–53. [[CrossRef](#)]
13. Subramanian, M.K.; Sasikumar, R.; Arasappan, R.K.; Pramod, R.; Murugesan, V. Microstructural administered mechanical properties and corrosion behaviour of wire plus arc additive manufactured SS 321 plate. *Proc. Inst. Mech. Eng. Part C J. Mech. Eng. Sci.* **2021**, *235*, 7627–7633.
14. Singh Kasana, S.; Pandey, O.P. Effect of heat treatment on microstructure and mechanical properties of boron containing Ti-stabilized AISI-321 steel for nuclear power plant application. *Mater. Today Commun.* **2021**, *26*, 1948. [[CrossRef](#)]

15. Kchaou, Y.; Haddar, N.; Hénaff, G.; Pelosin, V.; Elleuch, K. Microstructural, compositional and mechanical investigation of Shielded Metal Arc Welding (SMAW) welded superaustenitic UNS N08028 (Alloy 28) stainless steel. *Mater. Des.* **2014**, *63*, 278–285. [[CrossRef](#)]
16. Brooks, J.A.; West, A.J.; Thompson, A.W. Effect of weld composition and microstructure on hydrogen assisted fracture of austenitic stainless steels. *Metall. Mater. Trans. A* **1983**, *14*, 75–84. [[CrossRef](#)]
17. Chen, X.H.; Li, J.; Cheng, X.; He, B.; Wang, H.M.; Huang, Z. Microstructure and mechanical properties of the austenitic stainless steel 316L fabricated by gas metal arc additive manufacturing. *Mater. Sci. Eng. A* **2017**, *703*, 567–577. [[CrossRef](#)]
18. Zhang, C.H.; Zhang, H.; Wu, C.L.; Zhang, S.; Sun, Z.L.; Dong, S.Y. Multilayer functional graded stainless steel fabricated by laser melting deposition. *Vacuum* **2017**, *141*, 181–187. [[CrossRef](#)]
19. Hu, Q.X.; Miao, J.Y.; Wang, X.L.; Li, C.T.; Fang, K.W. Microstructure and Properties of ER50-6 Steel Fabricated by Wire Arc Additive Manufacturing. *Scanning* **2021**, *2021*, 7846116. [[CrossRef](#)] [[PubMed](#)]
20. Yin, Q.X.; Chen, G.Q.; Cao, H.; Zhang, G.; Zhang, B.G.; Wei, S.Z. Transformation law of microstructure evolution and mechanical properties of electron beam freeform fabricated 321 austenitic stainless steel. *Vacuum* **2021**, *194*, 110594. [[CrossRef](#)]
21. Tang, Y.B.; Shen, X.W.; Liu, Z.H.; Qiao, Y.X.; Yang, L.L.; Lu, D.H.; Zou, J.S.; Xu, J. Corrosion behavior of selective laser melted Inconel 718 alloy in NaOH solution. *Acta Metall. Sin.* **2022**, *58*, 324–333.